Journal of Low Temperature Physics (2020) 199:955–961
https://doi.org/10.1007/s10909-019-02304-5

TES Bolometer Arrays for the QUBIC B-Mode CMB Experiment

S. Marnieros, et al. ***[full author details at the end of the article]***

Received: 4 September 2019 / Accepted: 7 December 2019 / Published online: 7 January 2020
© Springer Science+Business Media, LLC, part of Springer Nature 2020

Abstract
QUBIC is a ground-based experiment aiming to measure the B-mode polarization of the cosmic microwave background. The developed instrument is an innovative two-frequency band bolometric interferometer that will operate at 300 mK with NbSi TES arrays. In this paper, we describe the fabrication process of the detectors.

Keywords Cryogenic detectors · Cosmic microwave background · Transition edge sensors

1 Introduction

Precise measurement of the light-polarization anisotropies in the cosmic microwave background (CMB) is a big experimental challenge, requiring state-of-the-art sensitive detectors, extended control of instrumental systematic effects and accurate subtraction of foregrounds emitted by the sky [1, 2]. QUBIC (Q&U Bolometric Interferometer for Cosmology) is an experiment designed to observe the B-modes of the CMB polarization with a setup able to control systematics with higher precision than usual imagers [3–5]. The instrument is a bolometric interferometer that will be deployed in 2020, at the Alto Chorrillos site in Argentina. It is equipped with two focal planes filtered at 150 GHz and 220 GHz and detectors based on time-domain SQUID-multiplexed transition edge sensor (TES) arrays. The definition of a reproducible and robust microlithography fabrication process of the arrays was a high-priority task for QUBIC.

2 Fabrication of the QUBIC Detectors

The QUBIC focal planes consist of an assembly of four TES arrays forming a light sensitive surface of approximatively 100 mm diameter. Each array has 248 active pixels with a pitch of 3 mm, and eight test pixels placed on the side of the detection area. The active pixels are composed of a suspended meshed membrane with a NbSi TES on its center, and a light absorption metallic grid. Several superconducting thin

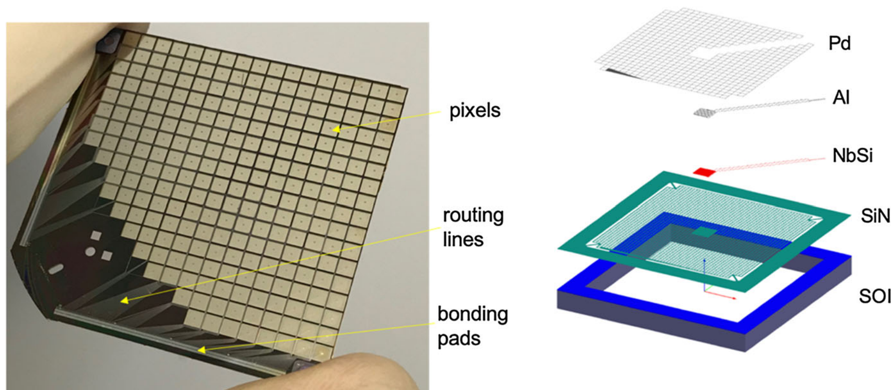

Fig. 1 Left, picture of a QUBIC 248-pixel TES array. Right, layout of the 3-mm pitch pixel structure. Pd grid for light absorption, NbSi for temperature sensing, SiN structure for decoupling the sensor from the cold bath and Al for routing the signal to the SQUID amplifiers (Color figure online)

lines route the signals from the TES to a series of bonding pads on the side of the array (Fig. 1). In the following, we give a detailed description of the array fabrication process.

2.1 SOI Substrates

The QUBIC arrays are manufactured using 3-inch-diameter SOI (silicon on insulator) substrates. Wafer maximum dimension is limited by our e-beam evaporation bench for deposition of the NbSi TES thin films. The SOI substrates are double-side polished and composed of three different layers whose thickness can be adjusted on request. In our case, we order a 5 μm crystalline Si device-layer, a 1 μm SiO_2 buried thermal oxide and a 500 μm crystalline Si handle wafer. Use of SOI-type wafers for QUBIC is essential in order to control the deep etching of the substrate related to the manufacture of the suspended membranes. The recipe is adjusted for high etching selectivity between Si and SiO_2, allowing to precisely remove the 500 μm handle-Si below the pixels. The SiO_2 acts as a barrier to stop etching and avoid removal of the remaining 5 μm Si device-layer. On top of this latter, an additional coating of 1-μm-thick silicon nitride (SiN) is used to fabricate the suspended membranes. SiN membranes have very weak thermal conductivity at low temperature, being therefore well-suited for low-background CMB detector arrays. The SiN coating is realized by LPCVD (low-pressure chemical vapor deposition) in order to get reproducible super-low-stress layers, with tensile stress below 100 MPa. SOI substrates with SiN coating on both sides are delivered by a Si-wafer manufacturer.

2.2 Routing and TES

The transition edge sensors, the routing lines and the bonding pads of the QUBIC arrays are realized in a common step based on the structuring of an evaporated bilayer.

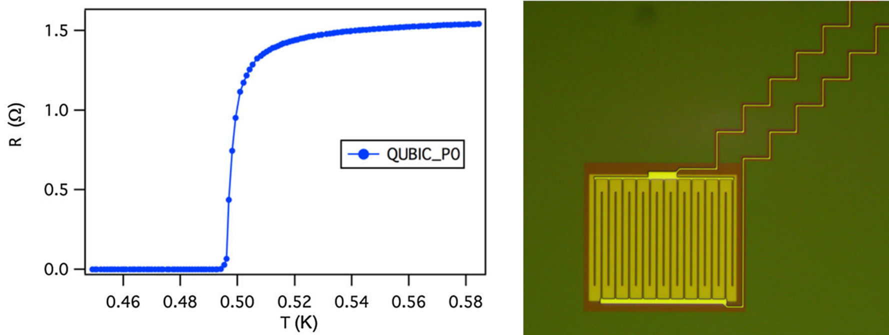

Fig. 2 Left, superconducting transition of a $Nb_{0.155}Si_{0.845}$ TES. Right, optical photo of a TES: light yellow = Al comb and routing with SiO coverage, dark yellow = NbSi with SiO coverage, brown = SiO. (Color figure online)

This latter consists of 30-nm-thick Nb_xSi_{1-x} deposited on the device-layer side of the SOI wafer, followed by 120 nm of Al. The bilayer is realized by e-beam co-evaporation of Nb and Si followed by e-beam evaporation of Al. It is important to keep the sample under vacuum between the two steps in order to avoid Nb_xSi_{1-x} oxide formation and get a high-quality proximity effect between the two layers. With the above-mentioned thicknesses, the bilayer behaves very similarly to pure aluminum and is used for the routing and contact pads. Its transition temperature lies systematically between 1.1 and 1.2 K. The TES are made of pure Nb_xSi_{1-x}, by selectively removing the Al top layer in the center of the pixels. We use a commercial Al wet etchant (MicroChemicals ANPE 80/5/5/10) that has a very high etching selectivity between Al and Nb_xSi_{1-x}.

The Nb_xSi_{1-x} is an amorphous layer showing superconducting behavior for Nb concentrations x higher than 0.13. Its superconducting transition temperature (T_c) increases with Nb concentration and can thus be controlled upon our needs [6, 7]. For the QUBIC 220 GHz focal plane, the concentration is adjusted to 0.155 ($Nb_{0.155}Si_{0.845}$) resulting in a T_c close to 500 mK (Fig. 2). Homogeneity of the Nb_xSi_{1-x} composition across each wafer and reproducibility between wafers is crucial in order to get pixels with matched T_c and signal sensitivities.

Use of NbSi–Al bilayers results in negligible contact impedance between the TES and the routing, simplifying considerably the lithography process. Due to the relatively high density of narrow lines (few microns), lithography of the routing layer is crucial. Any defect at this stage can interrupt a few routing lines reducing substantially the yield of operating pixels. To avoid dust contamination, the routing is realized as a first step of our lithography process by lift-off. The SOI wafer is spin-coated with AZ5214 resist on its device-layer side. The routing patterns of the resist, after mask exposure and development, are observed under a microscope in order to operate a quality control and check if the yield of operating pixels is high enough ($> 90\%$) to proceed to the bilayer deposition. After lift-off of the NbSi-Al bilayer, the routing lines and the contact pads are visible. The TES appear during a second step dedicated to a selective Al wet etching. A patterned S1813 photoresist prevents Al etching of the routing and pads during this step.

The square resistivity of a 30-nm $Nb_{0.155}Si_{0.845}$ film above its superconducting transition temperature is close to 600 Ohms, typically three orders of magnitude higher than usual TES. This is due to the fact that the Nb_xSi_{1-x} is a disordered amorphous alloy. In order to match to the noise of a SQUID amplifier, the normal state resistivity (R_n) of a TES must be of the order of 1 Ohm or lower. To solve this problem, the routing is extended on the top of our $240 \times 280\ \mu m^2$ NbSi TES in the form of a comb electrode structure (Fig. 2). By using two interleaved superconducting combs, our TES is separated into twenty sectors that are voltage-biased in parallel. Compared to a square TES geometry, this design reduces our sensor impedance by a factor of 400 and enhances the signal-to-noise ratio for SQUID amplification.

To avoid oxidation and damage from the etchants during the remaining steps of fabrication, the transition edge sensors and the routing lines are encapsulated with 25 nm of evaporated SiO. Coating of SiO can severely modify the stretch of our SiN membranes and must therefore be kept as thin as possible. Above 50 nm, deformation of the membranes is clearly visible and can result in a breakdown of the pixels. Lift-off lithography is used to avoid SiO coating of the pads at the end of the rooting lines. The detector array is connected to the SQUID-readout circuit via these pads, using ultrasonic bonding of 25 μm aluminum wires (wedge bonding).

2.3 Light Absorption Grid

Light absorption of the QUBIC arrays is based on a Pd grid placed in front of a reflecting surface at a distance of λ/4 to form an optical cavity resonator (λ being the photon wavelength). The grid design, realized by lift-off lithography, is adjusted to match the 377 Ohms square vacuum impedance in order to maximize light absorption efficiency. To obtain this, the grid filling factor is fixed to 10% and Pd thickness to 10 nm. The structure is protected by a final 25-nm-thick SiO coating. For 150 GHz photons, the grid must be placed in front of the reflecting surface at a distance of 500 μm. The thickness of the SOI wafers is chosen to match this distance, the reflecting surface being the metallic back-holder of the arrays. At 220 GHz, the optimum thickness of the wafers is smaller. Further information on the optical efficiency of the QUBIC instrument is available [3, 5].

2.4 Silicon Deep Etching

The remaining steps of the manufacturing process concern the fabrication of the suspended membranes. The following three etching steps are realized: a deep reactive ion etching (deep-RIE) of the 500-μm handle-layer using the Bosch process, a RIE to structure the SiN membrane in a shape of a suspended grid and a dry etching of the 5-μm device-layer.

The Si deep-RIE is operated by repeated cycles of SF_6 plasma etching and C_4F_8 passivation with typical etching rates of 3 μm per minute. This process produces vertical wall etching independently of the Si crystalline orientation, with a characteristic scalloped profile. It allows a flexible and easy design of the pixel cavities in the wafers. A 10-μm-thick AZ4560 resist is applied on the back side (handle-layer) of the SOI

substrate and mask developed to a pattern of 3-mm pitch squares (2.7 mm size squares separated by 300 μm walls). The front side coatings are protected during this step with S1813 resist. The SOI is then mounted onto a 4-inch carrier Si-wafer using vacuum oil to ensure high thermal coupling and avoid overheating by the plasma etching. The carrier wafer is cooled at 5 °C during processing. The backside SiN coating and the SiO_2 buried oxide layers are etched by switching the machine to a CHF_3 plasma recipe. The SOI is finally removed from the carrier wafer with care to avoid damage of the pixels and then cleaned with acetone and isopropanol. This deep-RIE step is also used to cut the wafer to a square shape, allowing the assembly of four arrays on each focal plane.

2.5 Suspended SiN Membranes

To realize the SiN-suspended grid, we use a CHF_3–CF_4 plasma RIE followed by a XeF_2 dry etching. Despite its fragility, the wafer is first spin-coated with S1818 resist, mask-exposed using the membrane grid pattern and developed in liquid AZ developer. It then undergoes the RIE that shapes the SiN layer to a meshed membrane, standing on top of the 5-μm Si device SOI-layer. The Si device is finally removed using XeF_2 dry etching. The S1818 resist is not dissolved prior to this etching in order to protect all previously deposited layers. XeF_2 gas allows homogenous attack of the device-layer without damaging the SiN membranes. The membranes are finally released and must not be immersed into liquid anymore to avoid damage by capillary forces. The remaining resist on the top of the sample is removed by O_2 plasma etching, and the array becomes available for low-temperature calibration and integration into the QUBIC instrument. The measured noise equivalent power (NEP) of these arrays is of the order of 5×10^{-17} W/sqrt(Hz) at 150 GHz, and the membrane thermal decoupling is typically 100 pW/K for 500 mK TES [8].

3 Conclusion

The QUBIC instrument is based on an assembly of 248-pixel arrays whose manufacture is now well-mastered. The pixels have a classical architecture of suspended meshed membranes for decoupling and NbSi TES that are thermally coupled to a grid for light absorption. Eight of these arrays will be integrated on the final QUBIC instrument to operate the 150 GHz and 220 GHz focal planes.

References

1. M. Kamionkowski, E.D. Kovetz, Annu. Rev. Astron. Astrophys. **54**, 227–269 (2016). https://doi.org/10.1007/s10909-015-1308-8
2. P.A.R. Ade et al., Phys. Rev. Lett. **121**, 221301 (2018). https://doi.org/10.1103/PhysRevLett.121.221301
3. A. Mennella et al., Universe **5**, 42 (2019). https://doi.org/10.3390/universe5020042
4. M.-A. Bigot-Sazy et al., Astron. Astrophys. **59**, 1–11 (2013). https://doi.org/10.1051/0004-6361/201220429
5. M. Piat et al., J. Low Temp. Phys. (under review)

6. C. Marrache-Kikuchi et al., Nucl. Instrum. Methods **A559**, 579 (2006). https://doi.org/10.1016/j.nima.2005.12.073
7. O. Crauste et al., J. Low Temp. Phys. **163**, 60–66 (2011). https://doi.org/10.1007/s10909-010-0284-2
8. M. Salatino et al., SPIE Proc. **10708**(1070845), 12 (2018). https://doi.org/10.1117/12.2312080

Publisher's Note Springer Nature remains neutral with regard to jurisdictional claims in published maps and institutional affiliations.

Affiliations

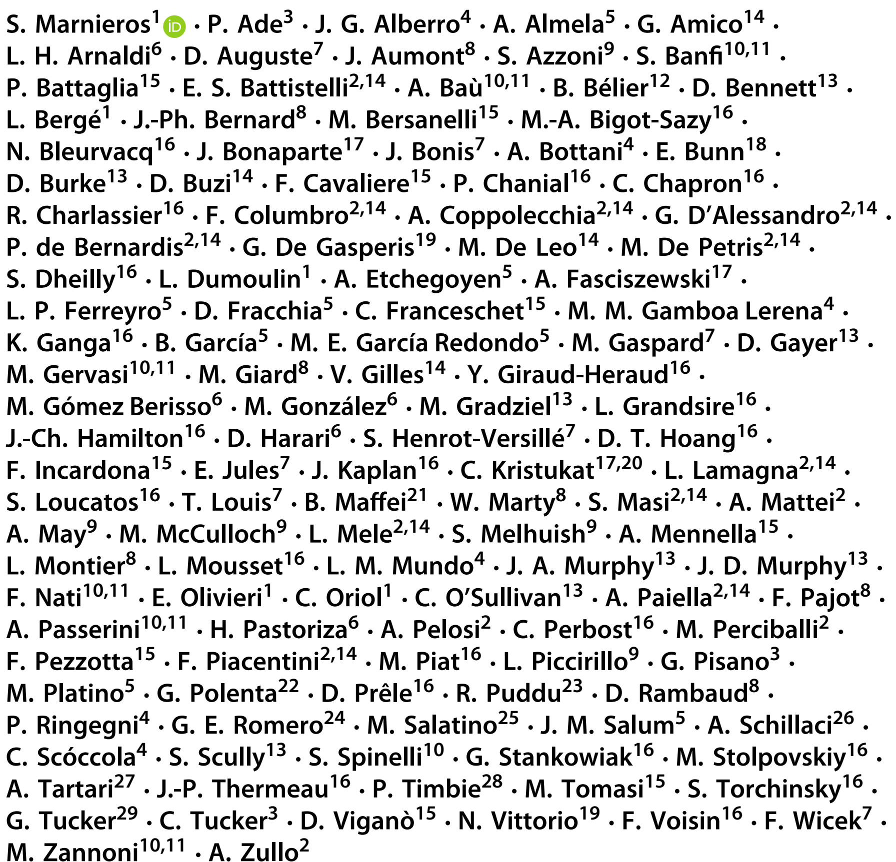

S. Marnieros[1] · P. Ade[3] · J. G. Alberro[4] · A. Almela[5] · G. Amico[14] · L. H. Arnaldi[6] · D. Auguste[7] · J. Aumont[8] · S. Azzoni[9] · S. Banfi[10,11] · P. Battaglia[15] · E. S. Battistelli[2,14] · A. Baù[10,11] · B. Bélier[12] · D. Bennett[13] · L. Bergé[1] · J.-Ph. Bernard[8] · M. Bersanelli[15] · M.-A. Bigot-Sazy[16] · N. Bleurvacq[16] · J. Bonaparte[17] · J. Bonis[7] · A. Bottani[4] · E. Bunn[18] · D. Burke[13] · D. Buzi[14] · F. Cavaliere[15] · P. Chanial[16] · C. Chapron[16] · R. Charlassier[16] · F. Columbro[2,14] · A. Coppolecchia[2,14] · G. D'Alessandro[2,14] · P. de Bernardis[2,14] · G. De Gasperis[19] · M. De Leo[14] · M. De Petris[2,14] · S. Dheilly[16] · L. Dumoulin[1] · A. Etchegoyen[5] · A. Fasciszewski[17] · L. P. Ferreyro[5] · D. Fracchia[5] · C. Franceschet[15] · M. M. Gamboa Lerena[4] · K. Ganga[16] · B. García[5] · M. E. García Redondo[5] · M. Gaspard[7] · D. Gayer[13] · M. Gervasi[10,11] · M. Giard[8] · V. Gilles[14] · Y. Giraud-Heraud[16] · M. Gómez Berisso[6] · M. González[6] · M. Gradziel[13] · L. Grandsire[16] · J.-Ch. Hamilton[16] · D. Harari[6] · S. Henrot-Versillé[7] · D. T. Hoang[16] · F. Incardona[15] · E. Jules[7] · J. Kaplan[16] · C. Kristukat[17,20] · L. Lamagna[2,14] · S. Loucatos[16] · T. Louis[7] · B. Maffei[21] · W. Marty[8] · S. Masi[2,14] · A. Mattei[2] · A. May[9] · M. McCulloch[9] · L. Mele[2,14] · S. Melhuish[9] · A. Mennella[15] · L. Montier[8] · L. Mousset[16] · L. M. Mundo[4] · J. A. Murphy[13] · J. D. Murphy[13] · F. Nati[10,11] · E. Olivieri[1] · C. Oriol[1] · C. O'Sullivan[13] · A. Paiella[2,14] · F. Pajot[8] · A. Passerini[10,11] · H. Pastoriza[6] · A. Pelosi[2] · C. Perbost[16] · M. Perciballi[2] · F. Pezzotta[15] · F. Piacentini[2,14] · M. Piat[16] · L. Piccirillo[9] · G. Pisano[3] · M. Platino[5] · G. Polenta[22] · D. Prêle[16] · R. Puddu[23] · D. Rambaud[8] · P. Ringegni[4] · G. E. Romero[24] · M. Salatino[25] · J. M. Salum[5] · A. Schillaci[26] · C. Scóccola[4] · S. Scully[13] · S. Spinelli[10] · G. Stankowiak[16] · M. Stolpovskiy[16] · A. Tartari[27] · J.-P. Thermeau[16] · P. Timbie[28] · M. Tomasi[15] · S. Torchinsky[16] · G. Tucker[29] · C. Tucker[3] · D. Viganò[15] · N. Vittorio[19] · F. Voisin[16] · F. Wicek[7] · M. Zannoni[10,11] · A. Zullo[2]

✉ S. Marnieros
Stefanos.Marnieros@csnsm.in2p3.fr

[1] CSNSM, CNRS/IN2P3, Université Paris-Saclay, Orsay, France

[2] Istituto Nazionale di Fisica Nucleare Roma A Section, Rome, Italy

[3] Cardiff University, Cardiff, UK

[4] Universidad Nacional de la Plata, Buenos Aires, Argentina

[5] Instituto de Technologías en Detección y Astropartículas, Buenos Aires, Argentina
[6] Ctr. Atómico Bariloche e Instituto Balseiro, CNEA, Buenos Aires, Argentina
[7] Laboratoire de l'Accélérateur Linéaire (CNRS-IN2P3), Orsay, France
[8] Institut de Recherche en Astrophysique et Planétologie (CNRS-INSU), Toulouse, France
[9] University of Manchester, Manchester, UK
[10] Università degli Studi di Milano Bicocca, Milan, Italy
[11] Istituto Nazionale di Fisica Nucleare Milano Bicocca section, Milan, Italy
[12] Centre de nanosciences et de nanotechnologies, Orsay, France
[13] National University of Ireland, Maynooth, Ireland
[14] Università di Roma La Sapienza, Rome, Italy
[15] Department of Physics, University of Milan, Milan, Italy
[16] Astroparticule et Cosmologie (CNRS-IN2P3), Paris, France
[17] Comisión Nacional De Energia Atómica, Buenos Aires, Argentina
[18] Richmond University, Richmond, VA, USA
[19] Università di Roma Tor Vergata, Rome, Italy
[20] Universidad Nacional de San Martn, San Martin, Argentina
[21] Institut d'Astrophysique Spatiale (CNRS-INSU), Orsay, France
[22] Agenzia Spaziale Italiana, Rome, Italy
[23] Pontificia Universidad Catolica de Chile, Santiago, Chile
[24] Instituto Argentino de Radioastronoma, Buenos Aires, Argentina
[25] Kavli Institute for Particle Astrophysics and Cosmology, Stanford, CA, USA
[26] California Institute of Technology, Pasadena, CA, USA
[27] Istituto Nazionale di Fisica Nucleare Pisa Section, Pisa, Italy
[28] University of Wisconsin, Madison, WI, USA
[29] Brown University, Providence, RI, USA